Highly efficient turbulent mixing in a weakly stratified abyssal boundary current

Kurt L. Polzin[1]†, T. Ijichi[1], A. C. Naveira Garabato[2], A. Forryan[2] and C. P. Spingys[2]

[1]Department of Physical Oceanography, Woods Hole Oceanographic Institution, Woods Hole, MA 02543, USA

[2]Ocean and Earth Science, University of Southampton, National Oceanography Centre, Southampton, SO14 3ZH, UK

(Received xx; revised xx; accepted xx)

The efficiency of turbulent mixing in a weakly stratified abyssal boundary current is assessed from observations of turbulence obtained with moored instrumentation and free-falling microstructure profilers. When scaled to represent potential energy, moored temperature spectra collapse onto the single-component velocity spectra from 3-axis current meters, and all spectra are consistent with a $-5/3$ inertial subrange. Application of inertial subrange formulas for downscale transports in 3-d turbulence yields a ratio of turbulent kinetic energy transport to turbulent potential energy transport of 0.8. This transport ratio is corroborated by microstructure measurements from free-falling profilers that return corresponding dissipation ratio estimates. Both metrics of mixing efficiency are substantially larger than the commonly accepted value of 0.2 for a standard shear production paradigm. The moored data depict a near-boundary mixing regime characterized by 'internal swash', entailing variability at diurnal and higher frequencies. We interpret the diagnosed high efficiency of near-boundary mixing to result from the action of internal swash on the weak ambient stratification, which does not allow sufficient time for the development of shear instabilities. Viewed overall, our finding of highly efficient mixing in an abyssal boundary current suggests a profound sensitivity of mixing efficiency to production-scale dynamics, and points to significant implications for the ocean's overturning circulation.

1. Introduction

1.1. *Motivation*

The overturning circulation of the global deep ocean (deeper than $\cong$ 2000 m) is critically shaped by the transformation of cold, dense, abyssal waters into warmer, lighter, mid-depth waters. Deep-ocean mixing is greatly enhanced in the vicinity of topography (e.g. Polzin *et al.* 1996, 1997), such that boundary mixing plays an important and possibly dominant role in sustaining deep-ocean overturning and diapycnal transformations. Considerable recent research (de Lavergne *et al.* 2016*a*; Ferrari *et al.* 2016; McDougall & Ferrari 2017; Ledwell 2018) has sought to understand the role of boundary mixing in determining the overturning circulation in general circulation models. The problem has been couched in terms of the influence of a no-normal buoyancy flux condition at the ocean floor. In combination with a relative maximum of buoyancy flux aloft, this implies (via a diapycnal advection - diffusion balance; McDougall (1987)) the occurrence of near-boundary upwelling, downwelling further above and, via vorticity

† Email address for correspondence: kpolzin@whoi.edu

conservation arguments, highly structured basin-scale flows along isopycnals in response to the diapycnal forcing.

While the adoption of an insulating boundary condition is incontrovertible given the relative unimportance of geothermal heating (Mashayek *et al.* 2017), an alternative perspective on the role of near-boundary mixing in deep-ocean overturning may be obtained from measurements of the rate of turbulent kinetic energy dissipation, ϵ. Turbulent dissipation is regularly assumed to be related to the buoyancy flux, $-g\overline{w'\rho'}$, via the turbulent kinetic energy (TKE) equation (Osborn 1980) which states that

$$\mathcal{P} = -\epsilon - g\overline{w'\rho'}, \tag{1.1}$$

where $\mathcal{P}$ is the rate of TKE production, (u, v, w) are velocity components in (x, y, z), g is gravity and ρ density. We refer the reader to Gregg *et al.* (2018) for a comprehensive review of the assumptions and nuances of this balance. In the context of (1.1), the buoyancy flux is typically parameterized as a fraction of the dissipation rate,

$$g\overline{w'\rho'} = K_\rho N^2 = \Gamma\epsilon, \tag{1.2}$$

where K_ρ is the diffusivity for buoyancy, $(-g\rho'/\rho_0)$, $N^2 = -g\rho_z/\rho_0$ a background buoyancy gradient with reference density ρ_0 and Γ is the dissipation ratio (often referred to as a 'mixing efficiency'). A similarly conceived production - dissipation balance of turbulent temperature variance (Osborn & Cox 1972) provides

$$K_\theta = \frac{\chi}{2\overline{\theta}_z^2}, \tag{1.3}$$

where θ is potential temperature, K_θ is the diffusivity for temperature and χ is the rate of dissipation of temperature variance. When the mixing rates of buoyancy and temperature can be taken as equal, the dissipation ratio may be quantified as

$$\Gamma = \frac{\chi N^2}{2\overline{\theta}_z^2 \epsilon} \, . \tag{1.4}$$

A fundamental feature of the no-normal buoyancy flux argument is the assumption of an upward increase of the buoyancy flux over a vertical scale of O(10-100) m, across a near-boundary zone where observations show that dissipation rates rise monotonically toward the ocean floor. Invoking (1.1-1.2), this assumption implies that the dissipation ratio Γ *must* tend to zero as the boundary is approached (Ferrari *et al.* 2016). This downward reduction in Γ is often argued to stem from the restriction on the development of 3-d turbulent overturns posed by the solid boundary's proximity (Holleman *et al.* (2016), see also Shaw *et al.* (2001); Gemmrich & van Haren (2002); Nash & Moum (2001) for additional observations), as well as from the increasing intensity of turbulence acting on weakening stratification (i.e. increasing buoyancy Reynolds number, $\epsilon/\nu N^2$, where ν is the kinematic viscosity) (Shih *et al.* 2005).

However rational this argument concerning the near-boundary suppression of turbulent length scales and the efficiency of near-boundary mixing might be, there are several reasons for disquiet. First, the observational evidence for decreasing Γ toward the seabed pertains only to shear-driven turbulence associated with a viscous bottom boundary condition. The relevance of this scenario for deep-ocean turbulence is far from obvious. Deep-ocean turbulence is particularly enhanced over steep and rough topography, as pressure gradients associated with flow negotiating topographic irregularities elicit acceleration and boost velocity gradients off the bottom boundary. Second, the extent to which near-boundary mixing efficiency is affected by time-dependent re-stratification processes, involving the exchange of mixed near-boundary waters with stratified interior

waters (Naveira Garabato *et al.* 2019), is poorly understood (Garrett 1979; Armi 1978). The question of how the spatio-temporal scales of this re-stratification process match with those required for the general circulation patterns enunciated in Ferrari *et al.* (2016) and de Lavergne *et al.* (2016*b*) to take hold is especially germane. Finally, it is unclear whether a reduced mixing efficiency near the boundary is actually required to close abyssal mass budgets. A simple examination of hypsometric effects associated with topographic variability (Polzin 2009; McDougall & Ferrari 2017; Ledwell 2018) suggests that the vertical structure of Γ as a function of height above bottom is not crucial for determining upwelling rates above a rough ocean floor.

In this work, we begin to shed light on the efficiency of near-boundary mixing in realistic deep-ocean environments by determining Γ in a paradigmatic constituent of the overturning circulation: an abyssal boundary current flowing along a steep topographic slope. We show that $\Gamma >> 0.2$ over a height in excess of 1000 m above the bottom. We argue that the primary factor explaining this highly efficient mixing is the sourcing of turbulent energy by a non-hydrostatic energy cascade initiated at scales far greater than those of overturning, rather than by shear instability as is commonly assumed.

1.2. *Regional Setting*

More than one quarter of the total Antarctic Bottom Water (AABW) exported northward from its formation regions in the subpolar Southern Ocean flows through Orkney Passage (OP; Garabato *et al.* (2002, 2014); Jullion *et al.* (2014)), a major gap in the ridge system bounding the Weddell Sea to the north (Fig. 1). AABW transport through OP is currently being monitored by an array of moorings, in place since 2012 (Abrahamsen *et al.* 2019). Prior to this phase of mooring-based monitoring, the area was surveyed with occasional hydrographic sections, one of which provided a control volume estimate of $K_\rho \cong 40 \times 10^{-4}$ m^2 s^{-1} for the AABW sufficiently dense to be trapped within the Scotia Sea (Heywood *et al.* 2002).

Motivated by the very intense mixing implied by this diapycnal transformation, we reviewed that work (Polzin *et al.* 2014*a*) in order to ascertain whether extant hydrographic and lowered acoustic Doppler current profiler (LADCP) data could illuminate the key mixing processes. We found that:

(1) Mixing rates in the far-field from the southern boundary of the Scotia Sea were an order of magnitude smaller than required to close the basin-integrated buoyancy budget.

(2) Mixing near the southern boundary of the Scotia Sea could possibly make an $O(1)$ contribution to the basin-integrated buoyancy budget only if (i) the highest buoyancy flux estimates obtained in OP occurred throughout the 700 km stretch of the abyssal boundary current flowing along the basin's southern boundary; or (ii) there existed substantial departures from widely accepted mixing metrics, such as $\Gamma = 0.2$, within the boundary current. Scenario (i) was not supported by available data. Scenario (ii) is examined in the present work.

Whether the basin's buoyancy budget is predominantly closed by far-field or boundary mixing is an important issue for the interpretation of ongoing climatic changes in AABW properties and volume (Abrahamsen *et al.* 2019). If mixing within the boundary current (Naveira Garabato *et al.* 2019) is dominant, it is likely that the intensity of the mixing and the diapycnal transformations it sustains will depend nonlinearly on the strength of the AABW flow. If, instead, mixing within the basin interior prevails, the intensity of the mixing is most probably contingent on velocity fluctuations induced by mesoscale eddies and tides that are independent (Abrahamsen *et al.* 2019) from the AABW transport .

This paper is organized as follows. The theoretical concepts underpinning our analytical approach, and the observational data considered here, are outlined in Section 2. In

Section 3, we present results of our analysis of the production, downscale cascade, and dissipation of TKE and temperature variance, on which our assessment of Γ is founded. A rationalization of the large Γ values inferred from our measurements is offered in Section 4, where we argue that the highly efficient mixing is caused by a short-circuiting of the shear instability that is normally invoked as a production process for 3-d turbulence.

2. Theoretical Background and Data

2.1. *Theoretical Background*

Our goals in this paper are to quantify the ratio of the rate of potential energy dissipation ($\chi N^2/2\overline{\theta}_z^2$) to the rate of TKE dissipation (ϵ) in a weakly stratified abyssal boundary current, and assess the reasons why this ratio is $\sim O(1)$ rather than the commonly assumed value of 0.2 (Gregg *et al.* 2018). In pursuing these goals, we will make a distinction between the ratio of dissipation rates measured at the scales in which molecular processes act irreversibly (which we will refer to as the *dissipation ratio*) and the ratio of the downscale transports of potential energy and TKE within an inertial subrange (which we will refer to as the *transport ratio*). Both of these ratios are metrics of the efficiency of mixing.

In the following, we provide a brief review of a series of theoretical notions that we will invoke to estimate dissipation and transport ratios from observations. We do this in order of increasing scale: from dissipation scales to production scales.

2.1.1. *Dissipation Scales*

The scales at which TKE and turbulent temperature variance dissipation occur are sampled using oceanic microstructure sensors. In order to achieve this, the sensors must resolve gradients on scales close to the Kolmogorov scale,

$$L_K = (\epsilon/\nu^3)^{1/4},$$

and the Batchelor scale,

$$L_B = (\epsilon/\nu\kappa^2)^{1/4},$$

where ν is the molecular viscosity and κ is the molecular diffusivity for temperature. L_K and L_B respectively define the smallest scales of turbulent fluctuations in velocity and temperature. The ratio between molecular viscosity and diffusivity is known as the Prandtl number, $P_r = \nu/\kappa$. L_K and L_B differ by the square-root of P_r, and $P_r \cong 12$ here. We thus expect there to be a limited range of wavenumbers for which viscosity damps velocity fluctuations, but temperature fluctuations are advected and distorted by straining motions at larger scales (i.e. there is a viscous-convective subrange in our microstructure data). The mixing efficiency Γ can be immediately appreciated from figures of microstructure shear and temperature spectra scaled by $N^2/\overline{\theta}_z^2$ (section 2.4) since the ratio of the peak shear and scaled temperature spectral levels in their respective dissipation ranges scales as $O(\Gamma\sqrt{P_r})$.

2.1.2. *The Inertial Subrange*

Our interpretation of measurements from both moored and vertical profiling instrumentation is based on Taylor's frozen-field hypothesis, by which the frequency of a turbulent fluctuation, σ, may be simply related to the fluctuation's one-dimensional wavenumber, k_1, through a low-passed horizontal velocity (in the mooring's case) or a vertical descent rate (in the profiler's case), U, i.e. $\sigma = k_1 U/2\pi$. This assumption readily enables a comparison of microstructure estimates of ϵ and χ with estimates of

those variables from inertial subrange formulas for turbulent velocity and temperature spectra, respectively given by

$$\Phi_{u,v,w} = 0.51\ [\frac{4-\cos^2(\gamma)}{3}]\ \epsilon^{2/3} k_1^{-5/3} \tag{2.1}$$

and

$$\Phi_\theta = 0.4\ \chi\ \epsilon^{-1/3}\ k_1^{-5/3}, \tag{2.2}$$

with

$$\phi^2 = \int_0^\infty \Phi(k_1) dk_1. \tag{2.3}$$

Here Φ denotes one-sided, one-dimensional wavenumber (k_1) spectra with variance ϕ^2. The factors of 0.51 in (2.1) and 0.4 in (2.2) are empirically determined constants from atmospheric measurements in unstratified boundary layers, summarized in Sreenivasan (1995, 1996). The factor $(4-\cos^2(\gamma))/3]$ in (2.1) assumes local isotropy, a condition that is satisfied when the buoyancy Reynolds number exceeds 200 (Gargett *et al.* 1984). The variable γ represents the direction relative to the prevailing low-passed / descent velocity, U. A value of $\gamma = 0$ corresponds to the streamwise velocity component; spanwise velocity component spectra are a factor of 1/3 greater.

An inertial subrange transport-based definition of Γ may be derived as follows. First, we introduce a ratio of the scaled velocity and temperature variance spectra defined in (2.1)-(2.3), as

$$R_s \equiv \frac{N^2 \Phi_\theta / \overline{\theta}_z^2}{\Sigma \Phi_{u,v,w}/3}\ . \tag{2.4}$$

Substituting (2.1)-(2.2) into (2.4), we have

$$R_s = 0.64 \frac{\chi N^2}{\epsilon \overline{\theta}_z^2}\ . \tag{2.5}$$

Finally, if we assume that the turbulent diffusivities for buoyancy (K_ρ) and temperature (K_θ) are equivalent, $K_\rho = K_\theta$, then (1.4) becomes

$$\Gamma = 0.78 R_s. \tag{2.6}$$

Thus, (2.6) provides a definition of the mixing efficiency from estimates of the inertial subrange transports of TKE and potential energy.

2.1.3. *Production Scales*

A dissipation-based metric of production scales in 3-d turbulence is the Ozmidov length,

$$L_O = (\epsilon/N^3)^{1/2},$$

which measures the scale for which there is a balance between gravity (via the buoyancy frequency, N) and the inertial forces of turbulence. A reasonable interpretation is that overturns, which can be quantified via a Thorpe scale metric,

$$L_T = (z'^2)^{1/2},$$

where z' denotes vertical displacements required to render a density profile statically stable, are free to grow to scales as large as those in which gravity becomes important. There is substantial discussion of the interplay between L_O and L_T in time-dependent

turbulent flows (e.g. Mater *et al.* 2015; Mashayek *et al.* 2017). In this work, however, we present estimates of ϵ and χ that are averaged over many overturning scales, such that changes in the relationship between L_T and L_O in time-dependent flows may be ignored. Our averages are 'bin averages' rather than 'patch averages'.

A further scale that will be relevant in our analysis of the observations is an internal wave band production scale, L_P, which may be significantly larger than L_O. Approximating the advected frequency $\sigma = k_1 U$, with the buoyancy frequency N, L_P is defined as

$$L_P = U/N.$$

This height scale characterizes the linear lee wave response to flow over small-amplitude topography in the hydrostatic, non-rotating regime and a variety of other phenomena, such as internal wave drag, hydraulic drag and flow blocking over finite-amplitude topography (e.g. Baines 1997). A similar height scale, $L_P f/\alpha N$, where α is the topographic slope and f is the Coriolis frequency, characterises arrested Ekman layers, such as may be present in an abyssal boundary current flowing over sloping topography (e.g. Garrett *et al.* 1993). The multiplicity of dynamical contexts in which L_P features is directly linked to the energetic constraints on those regimes.

2.1.4. *Limitations of Theoretical Approaches*

A caveat of the manipulations leading to (2.6) is the assumption that the $k^{-5/3}$ slopes of the velocity and temperature spectra in (2.1)-(2.2) are indicative of 3-d turbulence. These spectral slopes may also be compatible with other dynamical regimes, such as e.g. the inverse energy cascades of 2-d turbulence (Kraichnan 1967) and geostrophic turbulence (Rhines 1979), or the direct energy cascade that may occur in stratified turbulence (Lindborg 2006) and internal waves (Sukhatme & Smith 2008).

A key insight of this work is that the data presented are argued to portray a non-hydrostatic $k_1^{-5/3}$ regime at $k_1 \ll L_O^{-1}$, transitioning to a 3-d turbulent $k_1^{-5/3}$ regime at $k_1 = L_O^{-1}$. Non-hydrostatic conditions implicate internal wave dynamics defined by $O(1)$ isopycnal slopes and intrinsic timescales of $O(N^{-1})$, rather than the highly anisotropic hydrostatic stratified turbulence paradigm (Lindborg 2006; Riley & Lelong 2000). There is some analytic support for this implication from the techniques of wave turbulence, in which spectral power laws represent a scale-invariant hypothesis for integro-differential equations characterizing spectral transfers for a variety of weakly nonlinear wave systems, (e.g. Zakharov *et al.* 1992). Lvov *et al.* (2010) document the existence of such a stationary scale-invariant solution for hydrostatic non-rotating internal waves with horizontal and vertical wavenumber energy spectra of $k_h^{-1.7}$ and $m^{-1.7}$, respectively. Noting that $-5/3$ and -1.7 are similar, a review of the Lvov *et al.* (2010) numerics, and further work incorporating non-hydrostatic conditions and estimates of spectral transports, are clearly called for.

Regardless of the vagaries in interpretation, we can state the following. In the case of stratified turbulence, Lindborg (2006) argue that the empirical Kolmogorov and Corrsin constants in (2.1) and (2.2), respectively, are both 0.51, which in turn leads to a transport ratio $\Gamma = 1$. In the case of internal waves, the presence of a scale-invariant solution implies that the aspect ratio is independent of wavenumber magnitude. Given that horizontal kinetic energy and potential energy are identical in this hydrostatic, non-rotating limit, it is difficult to conceive a situation other than one in which potential and kinetic energy transports are equal, again leading to $\Gamma = 1$.

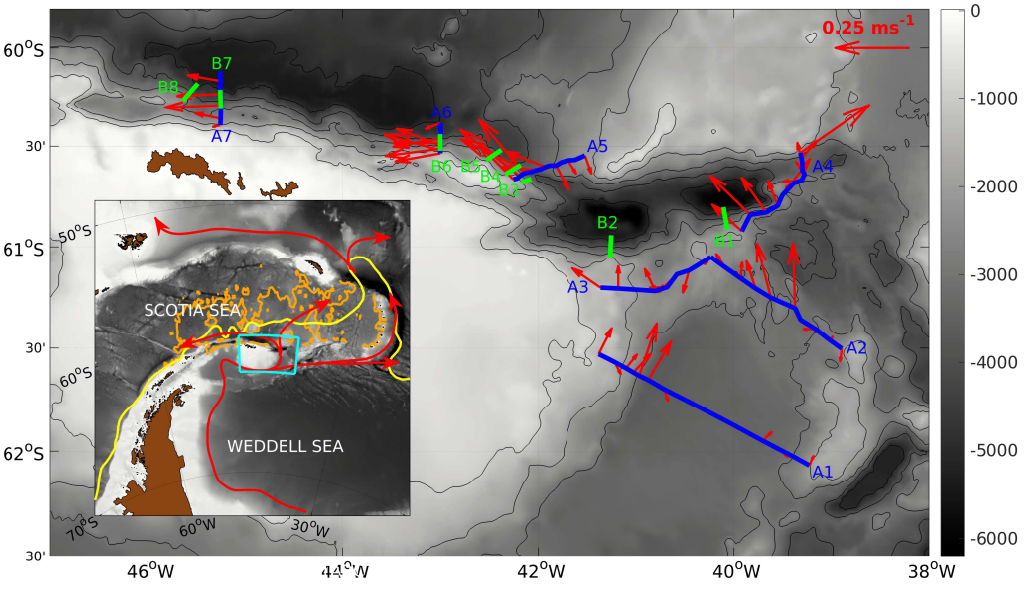

FIGURE 1. Regional setting for the abyssal boundary current in the Orkney Passage region, adapted from Naveira Garabato *et al.* (2019). The observational domain for the DynOPO process experiment is shown by the cyan outline in the inset large-area map, with major Antarctic Bottom Water (AABW) pathways indicated in red. Orange traces within the inset represent the grounding line for AABW with neutral density (Jackett & McDougall 1997) $\gamma^n \geqslant 28.31$ kg m^{-3} (Polzin *et al.* 2014*a*; Heywood *et al.* 2002), and yellow traces the southern boundary of the Antarctic Circumpolar Current (Orsi *et al.* 1995) referenced in the introductory narrative. Sections of measurements are marked by blue (coarse-resolution, A1-A7) and green (fine-resolution, B1-B8) lines in the main map. The mooring considered in this work was located on the 4140 m isobath along the A7-B7 sections. Observations of horizontal velocity averaged vertically over the AABW layer (defined by neutral density in excess of 28.26 kg m^{-3}) are indicated by red vectors. Bathymetry is denoted by grey shading in both maps.

2.2. *Observations*

A set of targeted measurements of the hydrographic, velocity and microstructure properties of the abyssal boundary current flowing through the OP region, between the Weddell and Scotia Seas in the Southern Ocean, was collected during expedition JR16-005 of RRS James Clark Ross between 20 March and 1 May 2017, supported by the UK - US Dynamics of Orkney Passage Outflow (DynOPO) project, Figure 1. The ship-based process experiment is discussed in Naveira Garabato *et al.* (2019), and is complemented by two moored elements. One of these elements entailed the deployment of a single mooring at 60°16.5′ S 45°15′ W, embedded within the AABW outflow from OP at a distance of approximately 150 km downstream of OP sill, along the southern boundary of the Scotia Sea (Figure 1). The mooring was equipped with 3-axis current meters, conductivity-temperature-depth (CTD) instruments and temperature sensors, which provided direct measurements of velocity and temperature fluctuations on turbulent time scales. Full details of the data set acquisition may be found in the JR16-005 cruise report (Garabato & et al. 2017).

In this work, we will analyse three components of the DynOPO measurement program: the mooring record introduced above; hydrographic profile data from a CTD / LADCP system lowered from the ship; and microstructure observations from a free-fall profiler. A description of each data type follows below.

2.2.1. *Moored Sensors*

The mooring considered in this work (Figure 1) consisted of 2 Nortek AquaDopps, 9 Modular Acoustic Velocity Sensors (MAVS), 10 SBE-37 CTD sensors and 20 SBE-39 temperature recorders, distributed along a 2000 m tall cable located in 4141 m water depth. The MAVS data were of limited duration due to unanticipated battery performance issues at cold temperatures. Otherwise, data return and quality were generally high. Calculating a mean velocity profile for the 7.5 days in which the majority of the current meters functioned correctly reveals a southwestward flow with a 15-20 cm s^{-1} westward component and a $\cong$ 5 cm s^{-1} southward component below 1000 m height above bottom, except at the bottom-most current meter. This deepest instrument, sited at a height of 65 m above the ocean floor, indicates a tendency for downslope flow, as expected from Ekman layer dynamics (Taylor & Sarkar 2008; Brink & Lentz 2010). This sensor appears to be at the very top of the nominal Ekman layer, with height scale $H_{\mathrm{Ekman}} = 0.4\sqrt{\tau/\rho}/f = 40$ m if one uses a standard quadratic drag parameterization of the bottom stress τ/ρ, drag coefficient of 2.5×10^{-3} and observed flow speeds of 0.2 m s^{-1}. See Appendix 1 for a detailed account of the moored resources.

The measurements of velocity and temperature fluctuations acquired by the moored sensors will be used to compute inertial-subrange wavenumber spectra of velocity, $\Phi_{u,v,w}$, and temperature, Φ_θ. To do this, we first rotate the velocity data into the record-mean streamwise / spanwise coordinate system. Second, we followed the lead of Shaw *et al.* (2001) to generalize the inertial subrange formulas (2.1)-(2.2) to include temporal aliasing, spatial averaging associated with a non-point sensor, and a white noise floor. This allows us to identify appropriate frequency bandwidths over which to generate robust inertial-subrange estimates of ϵ. Third, we combine this value of ϵ with (2.2) to produce an inertial-subrange estimate of χ. Further details are given in Appendix 1.

2.3. *Ship-Deployed CTD/LADCP System*

A standard hydrographic-quality SeaBird 911 CTD was lowered from the ship to obtain vertical profiles of pressure, temperature and salinity. Although the salinity data are contaminated by ship heave in ocean swell being communicated down the wire, resulting in noise at vertical wavelengths of 20 m and smaller, the data are of higher quality than those obtained using the unpumped SeaBird CTD on the free-falling VMP profiler described below. These wire lowered data were significant in the selection of data segments having limited variability in temperature-salinity characteristics, and thus limiting the contribution of isoypcnal stirring (Ferrari & Polzin 2005) to the thermal dissipation rate χ.

2.4. *Free-Fall Microstructure Profiler*

Microstructure data from a Rockland Scientific VMP-6000 profiler were reprocessed to specifically target an accurate estimation of dissipation ratio. In the standard processing of microstructure data, a piece length of 1 s is chosen and Fourier-transformed; spectral corrections are then applied, and quality control measures are implemented (based on e.g. agreement between variance estimates derived from duplicate sensors). In this standard approach, there tends to be less emphasis on quality control of temperature microstructure data, because a narrower segment of the temperature gradient spectrum is resolved than of the shear spectrum.

In contrast to this standard processing, our analysis of microstructure data utilized 4 s piece lengths, and averaged over depth bins of 10's to 1000 m of data from individual profiles. The choice of a larger piece length seeks to resolve more of the inertial-convective

subrange, and greater bin-averaging yields a smaller uncertainty in spectral estimates. The vertical extents of depth ranges contributing to bin-average spectra were determined by requiring a robust linear fit to the VMP-mounted CTD-derived potential temperature gradient. Data were furthered characterized in terms of water mass designations that serve as a proxy for height above bottom. These are, from bottom up, Antarctic Bottom Water (AABW), Lower Circumpolar Deep Water was divided into sections above (LCDW^{+}) and below (LCDW^{-}) a relative maximum in salinity associated with northern influences, and Upper Circumpolar Deep Water (UCDW), table 1 and Appendix 2.

The empirical Nasmyth spectrum for spanwise velocity gradients, and the viscous-convective / diffusive range passive scalar spectrum from Kraichnan (Bogucki *et al.* 2012), provided visual checks on data quality, and enabled quantification of instrument signal-to-noise ratios on these highly averaged spectra. The Kraichnan spectrum was additionally used to extrapolate the temperature variance at vertical scales smaller than that implied by the nominal temperature probe time constant (0.007 s). Further microstructure processing details are provided in Appendix 2.

3. Results

The central goal of this paper is to demonstrate the occurrence of highly efficient turbulent mixing in an abyssal boundary current, by showing that transport and dissipation ratios (estimated from inertial-subrange and dissipation-range measurements, respectively) are both of $O(1)$. To do this, we begin by examining the production of temperature variance from mooring-based observations in section 3.1. In section 3.2, we present transport ratios estimated from the moored measurements, and derive a corresponding vertical diffusivity profile. We conclude by providing microstructure-derived dissipation ratios and comparing them with the transport ratios, in section 3.3.

An important parameter in interpreting the results is the height of the sensor above bottom (H_{ab}). Atmospheric boundary layer data summarized in Kaimal *et al.* (1972) document the inception of a three-dimensional turbulent subrange at an Eulerian frequency of $\sigma = k_1 U = U/H_{ab}$, with turbulent production dominated by lower frequencies and larger horizontal scales. A simple interpretation is that three-dimensional eddies characterizing the inertial subrange are inefficient at communicating information about the bed stress from the bottom boundary. A second context is provided by transport ratios (2.1) estimated by Holleman *et al.* (2016). Using ship-mounted instrumentation they report a 'boundary influenced' regime of decreasing transport ratios (2.1) when $L_O/\kappa H_{ab} > 0.25$, in which $\kappa = 0.4$ is the von Karman constant in the context of log-layer similarity theory. If the dissipation range metric of overturning, L_O, is assumed to be three-dimensional, this condition for 'boundary influence' is represented as $k_1 U = U/2\pi L_O$ and the criteria for 'boundary influence' of buoyancy production becomes remarkably similar to the criteria for the transition between production scales to an inertial subrange. The H_{ab} thus informs about the range of frequencies over which to estimate transport ratios in a 3-dimensional cascade and interpretation of the results.

3.1. *Production*

An overview of the process underpinning the production of temperature variance in the abyssal boundary current environment sampled by the mooring is provided by Figure 2. The figure illustrates the evolution of potential temperature at depths instrumented with SBE-39 temperature recorders within the deepest 730 m of the water column (see Table 2) over a 3.5-day period, and reveals prominent variability at all depths with apparent diurnal (24 h) and inertial (13.8 h) periodicity. The most striking feature of

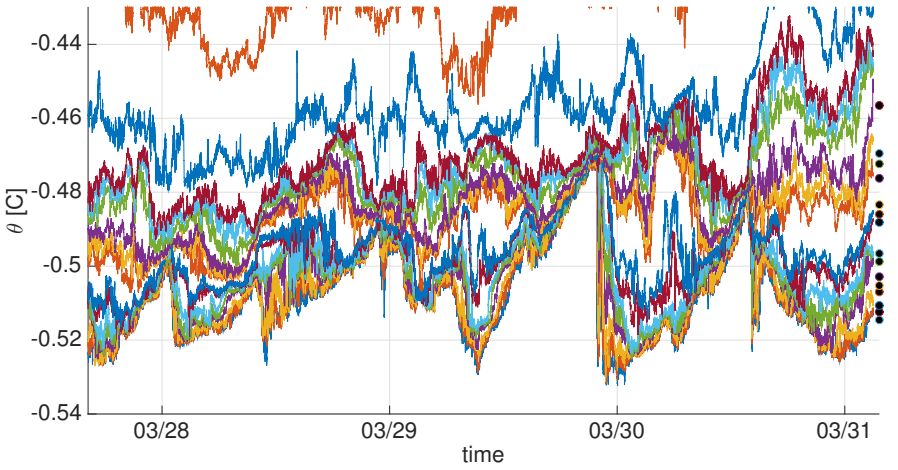

FIGURE 2. Time series of moored SBE-39 potential temperature traces over the bottom-most 1000 m of the mooring. Mean potential temperatures of the individual sensors are indicated by filled circles to the right. These sensors are not distributed uniformly in depth. Their heights above bottom are: 91 m, 117 m, 143 m; 201 m, 231.5 m, 262 m; 326 m, 356.5 m, 387 m (non-functional); 451 m, 481.5 m, 512 m; 577 m, 606.5 m, 635 m; 728; 891 m, See table 2. The non-uniform spacing explains the white space visible between groups of 3 traces.

the temperature variability is the recurrent (quasi-diurnal) pinching of traces over the bottom-most 600 m, indicative of very weak stratification. These are followed by abrupt transitions lasting 1-2 h, which imply re-stratification via an onslope rush of cold, dense water. The association between these abrupt transitions and high-frequency temperature variability denotes the occurrence of a turbulent flow field, rather than the passage of a front in geostrophic balance. In the remainder of this work, we term this production process 'internal swash' by analogy with swash, the turbulent layer of water that washes up on a beach after an incoming wave has broken. A working definition of the internal swash zone height scale is provided by the absence of stratification.

Next, we assess the rates of production of temperature variance effected by internal swash, by examining co-spectra of vertical velocity and temperature variability. We conduct this assessment at two levels: at 64 m above the ocean floor, a level embedded within the internal swash; and at 990 m H_{ab}, which is above the near-boundary internal swash zone as defined above, but is likely to be impacted by internal wave radiation from the swash zone.

At 64 m H_{ab}, production of temperature variance by the internal swash process is apparent at frequencies of 1-10 cpd (Fig. 3), for which a negative $w'T'$ co-spectrum is indicative of the mixing of upward-flowing cold waters with downward-flowing warmer waters. This frequency band maps visually onto the most prominent temperature fluctuations in Figure 2. Some modest ($O(10\%)$) re-stratification (indicated by a positive $w'T'$ co-spectrum) occurs at higher frequencies spanning the internal swash band and U/H_{ab}. A 3-d inertial-convective subrange sets in at even higher frequencies (as in atmospheric boundary layer measurements, e.g. Kaimal *et al.* (1972)). The rate of production may be estimated by integrating the $w'T'$ co-spectrum over frequencies greater than 1 cpd, yielding $\overline{w'T'}\,\bar{\theta}_z = -1.3\times10^{-5}$ C m s^{-1} $\times 2.9\times10^{-5}$ C m^{-1} $= 3.8\times10^{-10}$ C^2 s^{-1}. This is in agreement with an inertial-subrange transport estimate presented in section 3.2 of $\chi/2 = 3.8\times10^{-10}$ C^2 s^{-1}.

At 990 m H_{ab}, the $w'T'$ co-spectrum (Figure 4) exhibits some qualitative differences with that at 64 m H_{ab}. Low frequencies (less than f) are associated with a positive co-spectrum, unlike at 64 m H_{ab}. In turn, frequencies in the $f - 2f$ band exhibit a negative co-spectrum, indicative of downgradient temperature transport (mixing). Higher frequencies support re-stratification, which is more pronounced than at 64 m H_{ab}. An inertial subrange sets in again at higher frequencies (periods shorter than 20 minutes). As the low-frequency (below f) upgradient temperature transport is linked to the cross-slope temperature transport ($v'T'$, not shown) rather than to local production of temperature variance, the rate of production may not be unambiguously estimated from the $w'T'$ co-spectrum. Instead, we integrate the $w'T'$ co-spectrum backward in frequency to determine the frequency at which the integral agrees with the inertial-subrange transport estimate that will be diagnosed in section 3.2. Order of magnitude agreement is found at f, $[\overline{w'T'\theta}_z = -2.4 \times 10^{-6}$ C m s^{-1} $\times 2.4 \times 10^{-4}$ C m^{-1} $= 5.8 \times 10^{-10}$ C^2 s^{-1}, compared with $\chi/2 = 2.8 \times 10^{-10}$ C^2 s^{-1}] as might be expected from a scenario in which turbulence is fed by a process within the internal wave band. We believe the internal wave band turbulent production and dissipation at 990 m H_{ab} to be a signature of internal wave radiation from the internal swash zone and will pursue that analysis elsewhere.

3.2. *The Inertial Subrange*

Having characterized the production of temperature variance, we now assess transport ratios based on moored sensor measurements of the inertial subrange. We first examine spectra of the three components of velocity (u, v, w) (3) and of buoyancy-scaled temperature (4) for the two vertical levels considered in section 3.1. All spectral slopes are close to following a $-5/3$ power law in frequency, suggesting that the measured fluctuations may be interpreted to arise from a frozen field of turbulence being swept by the moored sensors. The spectra exhibit two further properties that inform our approach to estimate inertial-subrange transports:

(i) The spectra of all three components of velocity overlap approximately, implying that the observed turbulent flow is non-hydrostatic. The rationale for this conclusion is provided by the continuity equation, $\nabla \cdot \mathbf{u} = 0$, from which it follows that, if there is no intrinsic cancellation between the horizontal velocity gradients (such as in a geostrophically balanced flow), then

$$\frac{u}{\ell} \sim \frac{w}{h}.$$

Here, u and w respectively denote scale estimates of horizontal and vertical velocity perturbations, and ℓ and h are the associated horizontal and vertical scales. An approximate equivalence between u and w indicates that $h \sim \ell$, implying that the flow is non-hydrostatic. Note that three-dimensional turbulence is non-hydrostatic, but non-hydrostatic motions need not be three-dimensional turbulence (e.g., part of the spectrum may be dominated by non-hydrostatic internal waves at intrinsic frequencies near N).

(ii) The scaled temperature spectra are consistent with a $k^{-5/3}$ power law not just on scales smaller than the Ozmidov scale, L_O (denoting a transition to 3-d turbulence), but also on scales as large as the internal wave band production scale, L_P. This observational result places the headwaters of a cascade in association with stratified turbulence or internal wave dynamics; see section 2.1.4. As one expects from an inertial subrange, production estimates within $L_P < k_1^{-1} < L_O$ are characterized by minor ($O(10\%)$) contributions relative to those at 1-10 cpd (Figures 3 and 4).

Viewed together, (i) and (ii) indicate that the production of temperature variance occurs at scales as large as $L_P \cong U/N$, triggering a non-hydrostatic cascade that extends

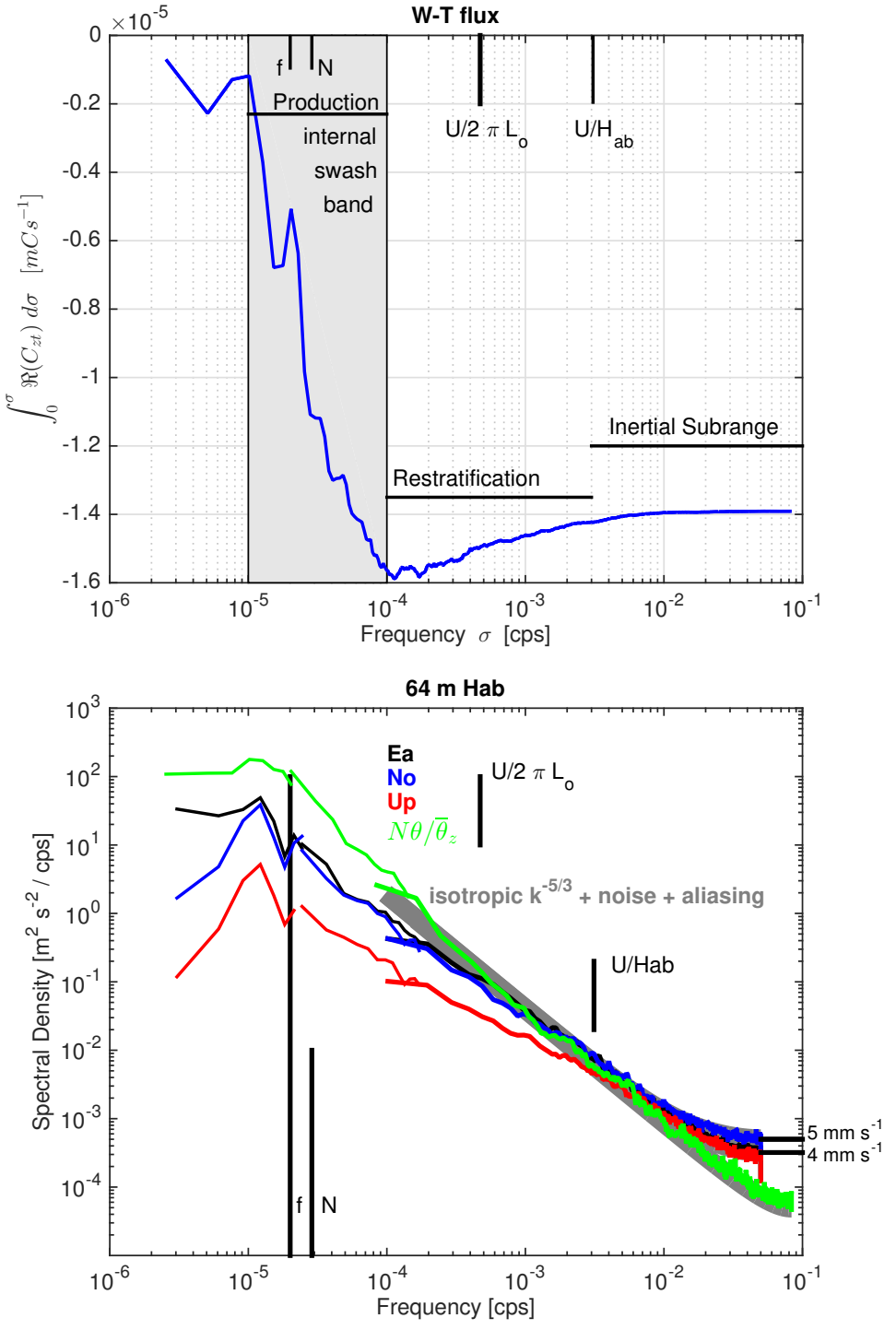

FIGURE 3. Upper panel: Vertical production at 64 m H_{ab}. The graph represents the running integral of the real part of the $w'T'$ co-spectrum. Black vertical lines indicate the Coriolis (f) and buoyancy (N) frequencies. Lower panel: Moored spectra of east/west (black), north/south (blue) and vertical (red) velocities, with temperature spectrum scaled by $N^2/\overline{\theta}_z^2$ (green). The grey shaded line represents the hypothesis of an isotropic $-5/3$ spectrum, with aliasing and a white noise model having rms levels posed to the right (see section 2.2.1 and Appendix 1.)

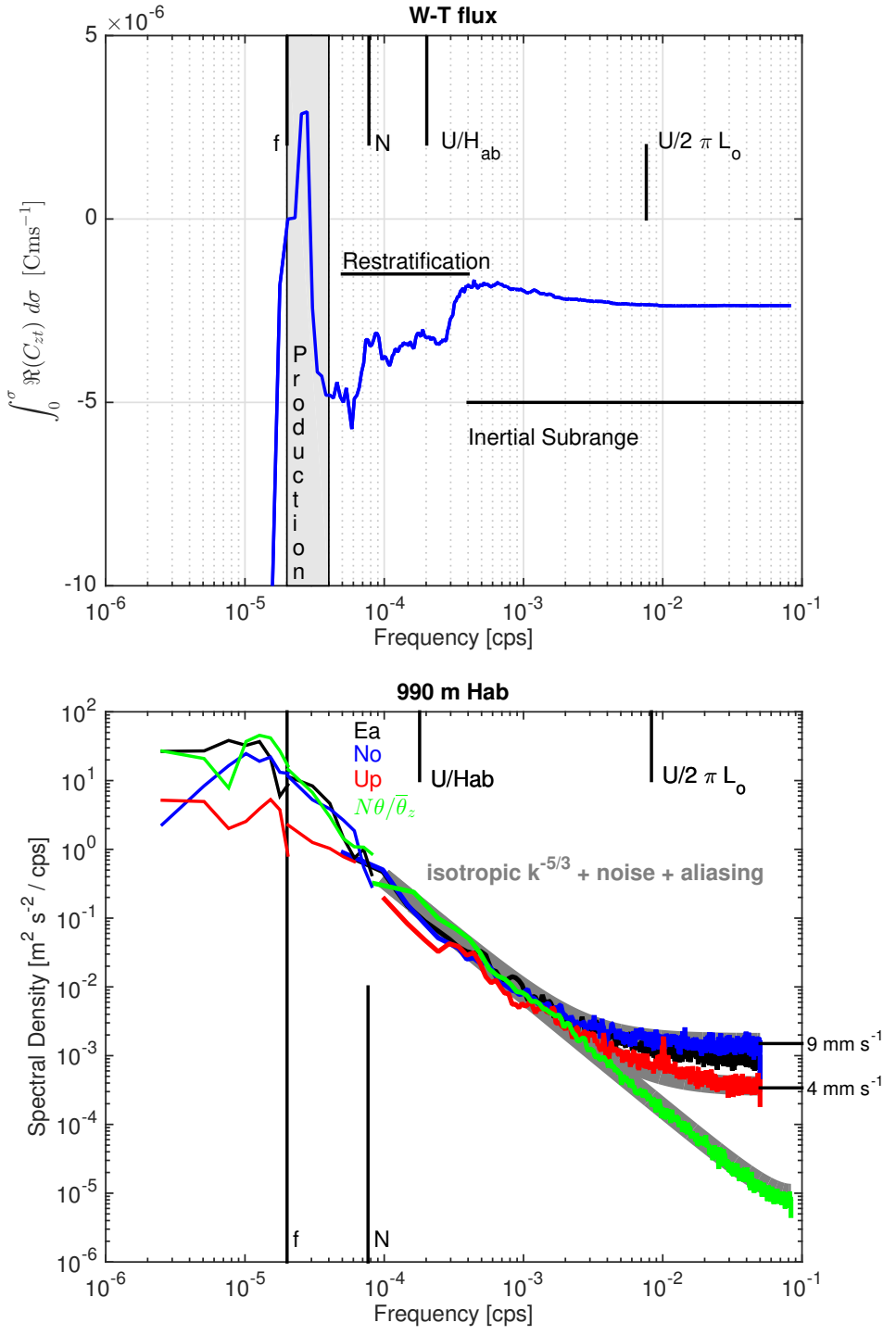

FIGURE 4. Upper panel: Vertical production at 990 m H_{ab}. The graph represents the running integral of the real part of the $w'T'$ co-spectrum. Black vertical lines indicate the Coriolis (f) and buoyancy (N) frequencies. Lower panel: Moored spectra of east/west (black), north/south (blue) and vertical (red) velocities, with temperature spectrum scaled by $N^2/\overline{\theta}_z^2$ (green). The grey shaded line represents the hypothesis of an isotropic $-5/3$ spectrum, with aliasing and a white noise model having rms levels posed to the right (see section 2.2.1 and Appendix 1).

across L_O. This motivates our subsequent application of inertial subrange formulas (2.1)-(2.2) on scales k_1^{-1} such that, above the internal swash zozne, $H_{ab} < k_1^{-1} < L_O$.

Next, we apply the inertial subrange expressions introduced in section 2.1.1 to the velocity and temperature spectra recorded by the moored instruments, in order to estimate time-mean vertical profiles of ϵ (2.1), χ (2.2), K_ρ (1.2) (using $\Gamma = 0.78R_s$ from (2.6) with the assumption of an approximate equality of velocity and buoyancy-scaled temperature spectra, i.e. $R_s = 1$) and K_θ (1.3) at the mooring site. The resulting profiles are displayed in Figure 5, alongside estimates of the time-mean squared gradient of potential temperature and time-mean squared buoyancy frequency. These reveal that ϵ and χ are enhanced downward by approximately one order of magnitude over the deepest 400 m of the water column, respectively reaching values of 2×10^{-8} W/kg and 7×10^{-10} C^2 s^{-1} near the bottom. Concurrently, vertical stratification is increasingly reduced as the boundary is approached over a $\cong$ 800 m-thick layer, with N^2 attaining a minimum of less than 10^{-7} s^{-2} near the ocean floor. Hydrographic casts obtained in deeper water maintain 4000-m stratification rates similar to those at 3000-m water depth, suggesting that this reduced stratification is a product of boundary mixing. While diffusivity values are largest (in excess of 1×10^{-1} m^2 s^{-1}) at the bottom and decay by over an order of magnitude to far-field values of $\approx 5 \times 10^{-3}$ m^2 s^{-1}, these far-field values are still three orders of magnitude greater than diffusivities associated with the background internal wavefield (Polzin *et al.* 2014*b*). Finally, mixing efficiencies are slightly smaller than 0.78 at 64 and 170 m H_{ab} and slightly greater than 0.78 above. Data from these bottom two current meters meet the definition of being 'boundary influenced' (Holleman *et al.* 2016) in that $L_O/\kappa H_{ab} > 0.25$.

Having calculated K_θ and K_ρ using $R_s = 1$, which is simply an expression of the empirical equivalence of buoyancy-scaled temperature and velocity component spectra, we find the diffusivity profiles to be in substantive agreement, both within and above the internal swash zone. We will next test this result against independent dissipation range estimates (section 3.3).

3.3. *Dissipation*

Here we estimate the dissipation ratio Γ from measurements of velocity and temperature microstructure. We consider stations for which the criteria outlined in section 2.2 and Appendix 2 are met, and re-process the local microstructure data to obtain spectra of vertical shear u_z and temperature gradient T_z, as exemplified by Figure 6. By integrating these spectra to obtain the gradient variances (u_z^2 and T_z^2) and assuming isotropy, we estimate dissipation rates as $\epsilon = 7.5\nu u_z^2$ and $\chi = 6\kappa T_z^2$, where ν and κ respectively denote the molecular viscosity and diffusivity. The dissipation ratio Γ is then derived from these dissipation-range variables by asserting that the mass diffusivity (K_ρ)and thermal diffusivity (K_θ) are equal, $\Gamma = \chi N^2/2\overline{\theta}_z^2\epsilon$ (Osborn 1980).

A synthesis of the resulting Γ values is provided in Figure 7, where dissipation-range Γ estimates (shown by black symbols) are displayed alongside inertial-subrange Γ estimates (shown by red symbols). Γ values are plotted as a function of the buoyancy Reynolds number, R_{eb}, with which Γ has been argued to scale inversely as indicated by the numerical results of Shih *et al.* (2005) (black curve). Three key features stand out. First, there is a broad agreement between dissipation-range and subinertial-range estimates of Γ. Second, our Γ estimates are not inconsistent with a trend toward cannonical values of 0.2 in the upper 500 m (see UCDW and LCDW^+ symbols and table 1). Third, there is a tendency for Γ to increase to $O(1)$ as the ocean floor is approached (LCDW^- and AABW symbols) and with increasing R_{eb} that disagrees with the (Shih *et al.* 2005) prediction.

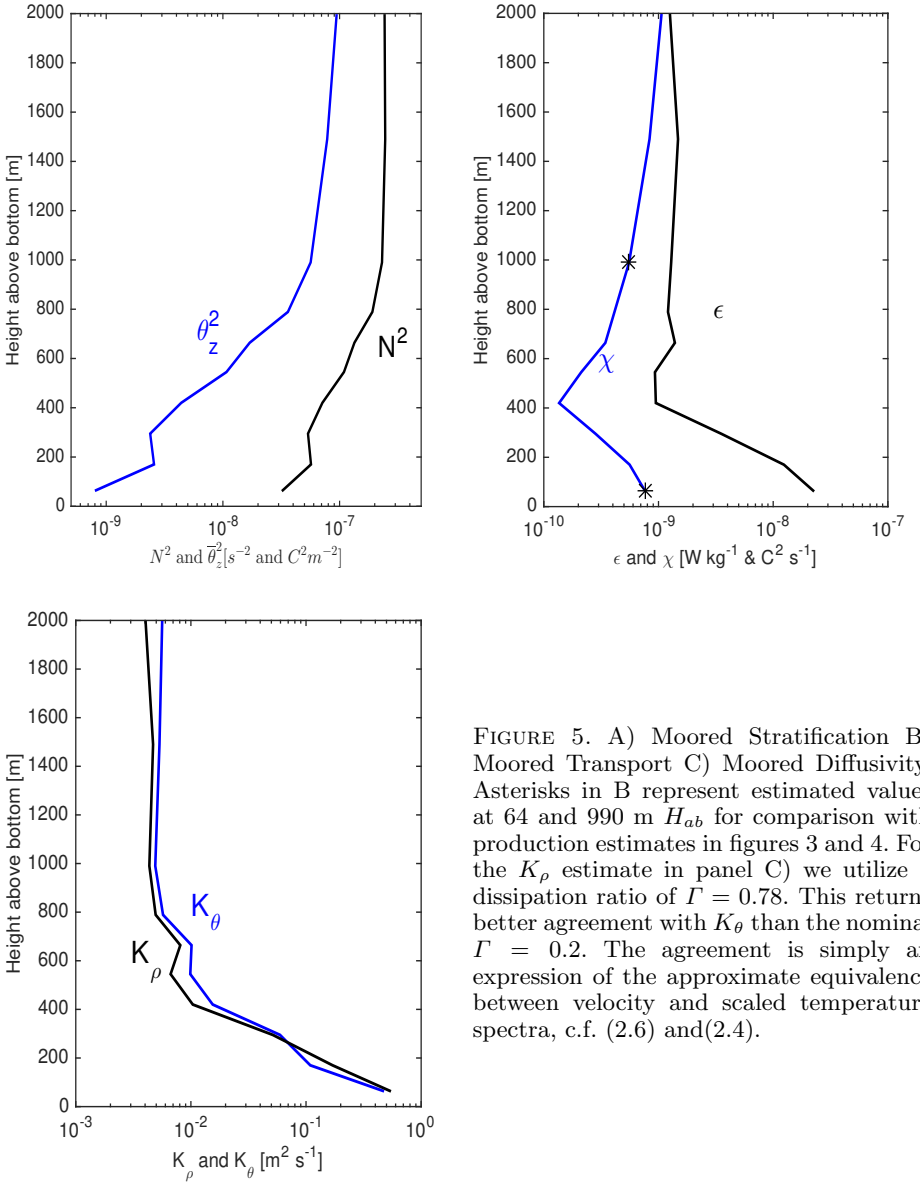

FIGURE 5. A) Moored Stratification B) Moored Transport C) Moored Diffusivity. Asterisks in B represent estimated values at 64 and 990 m H_{ab} for comparison with production estimates in figures 3 and 4. For the K_ρ estimate in panel C) we utilize a dissipation ratio of $\Gamma = 0.78$. This returns better agreement with K_θ than the nominal $\Gamma = 0.2$. The agreement is simply an expression of the approximate equivalence between velocity and scaled temperature spectra, c.f. (2.6) and(2.4).

Thus, our measurements support the notion that the efficiency of turbulent mixing increases (rather than decreases) as turbulence intensifies and stratification weakens near topography. The processes underpinning this surprising result are discussed in the following section. See table 1 for averaged estimates.

4. Discussion and Conclusions

The presence of a mean flow over sloping topography, such as is considered in this work, promotes several expectations that turbulence might be less energetic and mixing less efficient than generally in the ocean interior. When mean flow is oriented in the same direction as Kelvin wave propagation (i.e. with shallower topography to the left

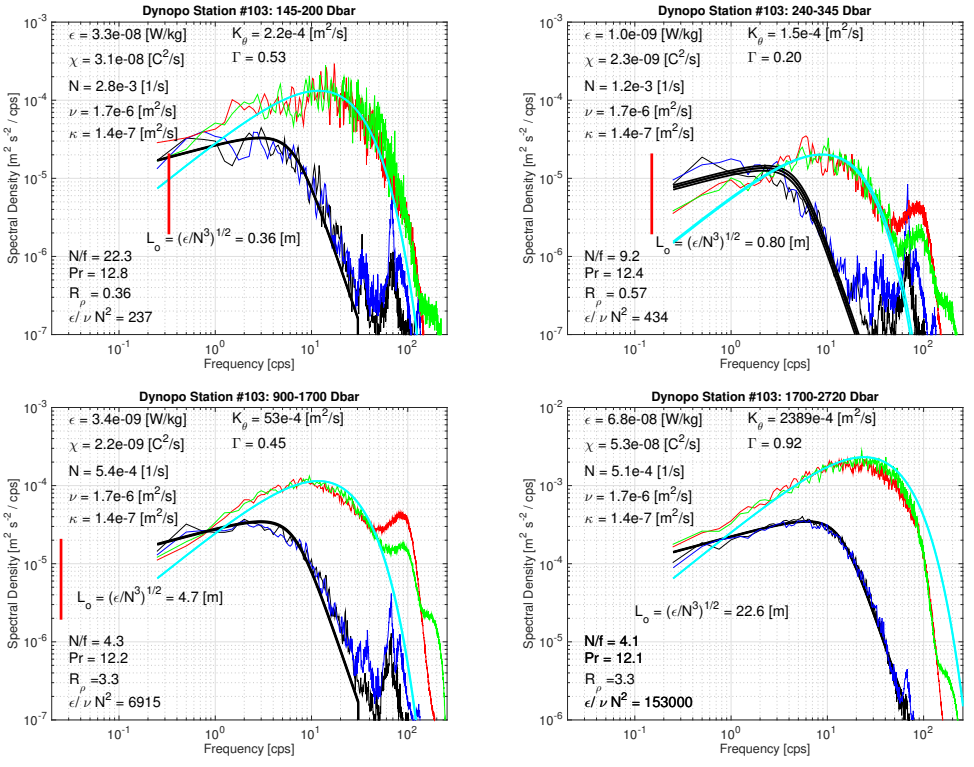

FIGURE 6. Vertical gradient spectra from the VMP data of DynOPO station 103. Black and blue data traces represent data from the two shear probes. Red and green data traces represent data from the (buoyancy-scaled) temperature sensors. Solid black and cyan curves indicate the Nasmyth and Kraichnan spectra, respectively, for the corresponding gradient variances. The graphs are arranged so that depth increases from upper left, upper right, lower left to lower right. These depth-averaged spectra are from UCDW, LCDW$^-$, LCDW$^+$ and AABW water mass classes, respectively. Posted within the graphs are the physical constants, non-dimensional parameters and key diagnostics.

TABLE 1. Summary of dissipation metrics appearing in Figure 7. There is some overlap between depth ranges, due to sloping water mass-defining isopycnals across the boundary current, and occasional overlap of depth bins between UCDW and LCDW$^+$ classes. Two estimates of Γ and R_{eb} are provided. The first represents a water mass average. The second, in parentheses, is an average of the depth bin-averaged metrics that appear in Figure 7.

Watermass	depth range	points	N/f	K_θ	Γ	R_{eb}
UCDW	110 - 290	1144	21	2.0×10^{-4}	0.25 (0.32)	414 (406)
LCDW$^+$	160 - 360	920	10.3	7.4×10^{-4}	0.37 (0.34)	309 (349)
LCDW$^-$	625 - 1780	11655	4.4	22×10^{-4}	0.47 (0.55)	2278 (2470)
AABW	1360 - 4542	31231	3.9	219×10^{-4}	0.80 (0.72)	16896 (12802)

in the Southern Hemisphere), a viscous condition of no flow at the bottom boundary is anticipated to trigger a downslope mass and buoyancy transport within an Ekman layer, leading to a reduction in the near-bottom flow and a decrease in drag (a steady-state paradigm known as the arrested Ekman layer (Garrett *et al.* 1993; Brink & Lentz 2010)). Over this same sector of sloping topography, a no-normal buoyancy flux condition is argued to induce the emergence of a relative maximum in the vertical profile of the

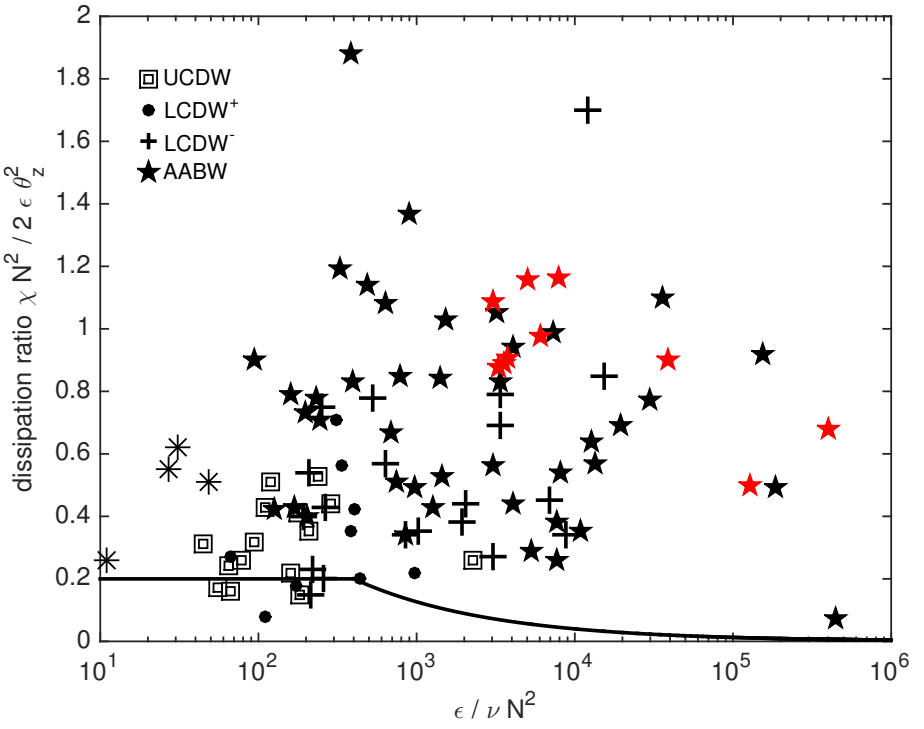

FIGURE 7. Estimates of dissipation ratio Γ vs. buoyancy Reynolds number $R_{eb} = \epsilon/\nu N^2$. Symbols denote relative position within the water column: pentagons lie within Antarctic Bottom Water (AABW), + are within Lower Circumpolar Deep Water (LCDW) below the salinity maximum, • within LCDW above the salinity maximum, compound squares within the Upper Circumpolar Deep Water (UCDW), and ∗ denote data from above the winter mixed layer base (Winter Water). Red pentagons are inertial-subrange estimates from moored data within AABW. The moored data have monotonically increasing $\epsilon/\nu N^2$ with depth. Estimates from the two deepest moored sensors appear as outliers with respect to the cloud of dissipation data; however, while the moored data are time averages, the dissipation data represent depth averages of VMP microstructure measurements and so extend much further off the bottom. The axis limits exclude one data point.

turbulent buoyancy flux at O(10-100 m) above the bottom (Ferrari *et al.* 2016). Since turbulent dissipation rates typically increase monotonically toward the bottom boundary, a reduced dissipation ratio Γ would be implied precisely where dissipation is most intense.

In this work, we ask the reader to set aside these preconceived notions and focus upon the singular element that triggers the cascade of turbulent kinetic and potential energies in our weakly stratified, abyssal boundary current: internal swash. Internal swash manifests itself as rapid transitions between conditions in which isopycnals steepen to be nearly vertical, and re-stratification associated with dense cold water rushing up-slope over a height scale consistent with $L_P = U/N$ (Figure 2). Internal swash provides for the production of temperature variance on frequencies of 1-10 cpd (figure 3), where the lower bound coincides with a diurnal tide of modest ($\cong$ 1 cm s^{-1}) amplitude. This swash-related production sets the headwaters of an inertial subrange that, in turn, directly feeds the inertial subrange of 3-d turbulence (Figures 3 and 4). The initial, production-driven, inertial subrange has a non-hydrostatic character (Figure 4), yet does not itself support 3-d overturning. The dynamics are likely those of nonlinear internal waves rather

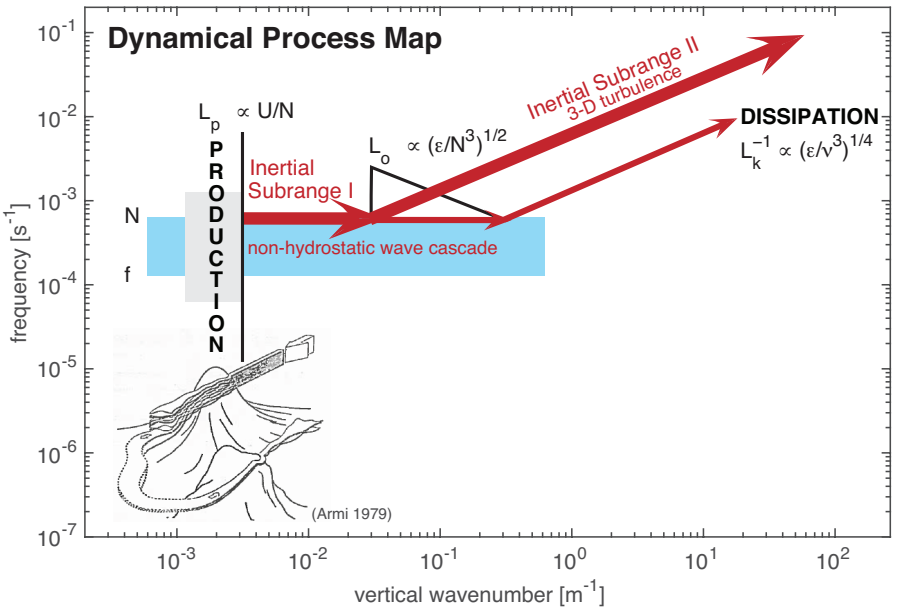

FIGURE 8. Schematic representation of the turbulent kinetic energy production and transport process described in this paper, rendered in intrinsic frequency and vertical wavenumber space. A production process with a height scale of L_P initiates a non-hydrostatic internal wave cascade. This cascade transfers energy downscale, to the point that overturning at a vertical scale of L_O initiates a second inertial subrange consisting of 3-d turbulence. This schematic is intended to complement and contrast with Figure 1 of Polzin *et al.* (2014*b*). A potential production process is that of topographic form drag, depicted in the thumbnail from Armi (1978).

than of stratified turbulence (section 2.1.4). Associated with the transition between subranges is an opportunity to reset inertial-subrange transport ratios. The observed continuity of temperature spectra across this transition (Figure 4) suggests that such a reset is not significant. Consequently, we infer transport ratios $\Gamma \cong 0.8$ that are broadly uniform across both subranges, and argue that these transport ratios appear unabated as dissipation ratios of $\Gamma \cong 0.8$. This newly documented mixing paradigm is graphically represented in Figure 8. Finally, mixing in this scenario is characterized by both a near-boundary increase in K_ρ, and diffusivities above the near-boundary zone of reduced stratification that are roughly 1000 times larger than values typical of the background internal wavefield ($K_\rho \cong 5 \times 10^{-6}$ m^2 s^{-1}) (Figure 5). Such elevated diffusivities above L_P imply vertical propagation, which could be effected by non-hydrostatic internal waves related to the internal swash process.

We believe that the high mixing efficiency revealed by our data set stems from the presence of weak stratification, which is characterized by $N/f \cong 4$ within the AABW layer and by even smaller values at the boundary. We suggest that a dynamical definition of 'weak stratification' may be constructed by analogy, as follows. Much of our understanding of oceanic internal waves is underpinned by observations at thermocline stratification rates with $N/f \cong 50$. In such data, vertical wavenumber spectra do not link up smoothly with turbulence observations but, rather, a transition regime occurs between vertical wavelengths of 10 m to 0.5 m (Gargett *et al.* 1981; Gregg *et al.* 1993; Polzin *et al.* 2003). The existence of this transition regime is arguably related to an instability process (Polzin 1996), which acts as an intermediary between downscale cascades induced

by internal wave-wave interactions at larger scales (Polzin & Lvov 2011) and by 3-d turbulence at smaller scales. There is an important disparity between the time scales governing the wave-wave dynamics and the instability dynamics. Specifically, Polzin (1996) argue that:

(i) The downscale energy transfer induced by wave-wave interactions scales as E^2N^2f, whereas the instability-mediated transfer scales as E^2N^3 (where E is a length-scale metric of the vertical-wavenumber spectral energy density at the vertical scales of the shear variance). Consequently, wave-wave interactions have a characteristically longer time scale (f^{-1}) than the instability process (N^{-1}).

(ii) Once the instability has been triggered, it takes some time for an unstable event to mix to completion. Data presented in Polzin (1996) suggest a mixing time scale of several buoyancy periods. This mixing time scale contrasts with the duration of an unstable event, as related to linear wave propagation. The duration of such an unstable event is arguably proportional to the inverse of f or, potentially, of the geometric mean of N and f, $\sqrt{Nf}$ (Garrett & Munk 1972).

(iii) The difference between the time scales of an unstable event and the ensuing mixing gives rise to a stratification dependence of the statistical distributions of shear variance, stratification and Richardson number, such that, with everything else being equal, fewer super-critical unstable events occur in the strongly stratified limit.

Polzin (1996) found indications of a transition to a weakly stratified parameter regime, but the evidence for such a transition in that work was not unambiguous. Here, however, a transition to a weakly stratified regime, in which the duration of unstable events is shorter than the mixing time scale, provides the most plausible explanation of our observations. This interpretation is supported by direct numerical simulations of Kelvin-Helmholtz billows developing from an otherwise steady parallel shear flow. These simulations document a time scale of 2-3 buoyancy periods to characterize the instability from roll up through dissipation and an event average mixing efficiency of $\Gamma \cong 0.2$ (e.g. Kaminski & Smyth 2019)

In our OP data set, buoyancy production is underpinned by diurnal and inertial frequencies which, when coupled to the low ambient values of N, result in an unstable event duration that is shorter than a mixing time scale. In other words, shear instabilities do not have sufficient time to roll up, develop secondary instabilities and mix to completion. The downscale energy cascade then proceeds via an alternative dynamical pathway. Our contention is that this alternative pathway is provided by the unabated extension of downscale transfers of internal wave (kinetic and potential) energy into 3-d turbulence.

Stepping back from our quantification of Γ, we (Naveira Garabato *et al.* 2019) have little doubt that the highly efficient mixing documented in this paper is, ultimately, an expression of the bottom boundary conditions in the abyssal boundary current flowing through the OP. The phenomenon that we label as internal swash, which starts at sub-inertial frequencies, may bear some resemblance to the time-dependent, super-inertial motions in the 1-d Ekman layer closure scheme presented by Brink & Lentz (2010). Notably, the bottom boundary conditions correspond to the configuration of a downwelling Ekman layer, and thereby provide a sink of Ertel potential vorticity. A growing literature associates a sign reversal in Ertel potential vorticity at the bottom boundary with the development of submesoscale instabilities (e.g. Wenegrat *et al.* 2018), where this interpretation is couched in terms of linear instability theory applied to a planar slope. On the basis of our results, we conjecture that the fundamental question may instead pertain to how external forcing, here in the guise of a diurnal tide, maps onto a finite-amplitude, internal swash process over a bottom boundary that departs from a uniform inclined plane.

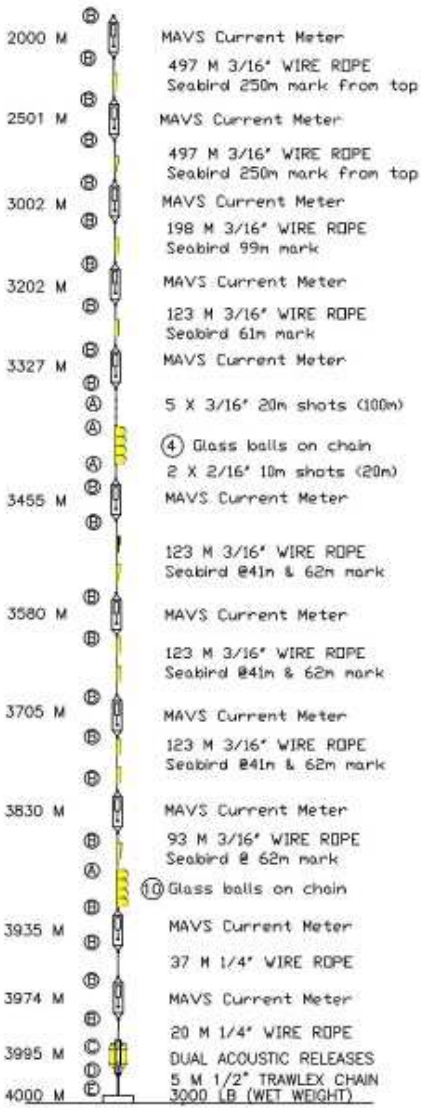

FIGURE 9. MooringDiagram

The DynOPO project is supported by the the US National Science Foundation (grants OCE-1536453 and OCE-1536779) and UK Natural Environment Research Council (grants NE/K013181/1 and NE/K012843/1). A.C.N.G. acknowledges the support of the Royal Society and the Wolfson Foundation. We are grateful to the scientific party, crew, and technicians on the RRS James Clark Ross for their hard work during data collection. Declaration of interests: The authors report no clonflict of interest.

5. Appendix 1: Moored instrumentation

The mooring considered in this work included four types of instrument, reviewed below.

Modular Acoustic Velocity Sensor (MAVS). The MAVS Thwaites & Williams (1996) is a specialized 3-axis acoustic travel time device with a single-ping intrinsic sensitivity of

TABLE 2. Summary of moored sensors and data return.

Height [m]	Sensor	Serial No.	variables	data return (days)	comments
1992	AquaDopp	11545	u,v,w,p	38.49	
	SBE-37	14634	t,c,p	38.46	out of memory
1742	SBE-39	0630	t		
1490	AquaDopp	11542	u,v,w,p	38.49	
	SBE-37	14638	t,c,p	38.46	out of memory
1240	SBE-39	0626	t		
990	MAVS	10290	u,v,w	7.84	
	SBE-37	14635	t,c,p	38.46	out of memory
891	SBE-39	0695	t		
789	MAVS	10297	u,v,w	8.16	
	SBE-37	5934	t,c,p	12.86	out of memory
728	SBE-39	0693	t		
664	MAVS	10295	u,v,w	30.79	
	SBE-37	14608	t,c,p	38.46	out of memory
635	SBE-39	0653	t		
606.5	SBE-39	0686	t		
577	SBE-39	0649	t		
545	MAVS	10299	u,v,w	3.22	
	SBE-37	14612	t,c,p	38.46	out of memory
512	SBE-39	0700	t		
481.5	SBE-39	0647	t		
451	SBE-39	0645	t		
420	MAVS	10289	u,v,w	7.59	Compass (Mx) ?able
	SBE-37	14644	t,c,p	38.46	out of memory
387	SBE-39	0688	t	non-functional	
356.5	SBE-39	0701	t		
326	SBE-39	0789	t		
295	MAVS	10288	u,v,w	3.43	
	SBE-37	14645	t,c,p	38.46	out of memory
262	SBE-39	0819	t		
231.5	SBE-39	0694	t		
201	SBE-39	0696	t		
170	MAVS	10296	u,v,w	9.60	'A' ducer dead
	SBE-37	14636	t,c,p	38.46	out of memory
143	SBE-39	0623	t		
117	SBE-39	0692	t		
91	SBE-39	0644	t		
65	MAVS	10298	u,v,w	9.69	
	SBE-37	14599	t,c,p	38.46	out of memory
26	MAVS	10355	u,v,w,t	17.79	'B' ducer dead, 'C' noisy
	SBE-39	0690	t		Not Recovered

0.3 mm s^{-1}. It is, in many respects, the oceanographic equivalent of a sonic anemometer, commonly used in atmospheric boundary layer studies. The effective noise in the current meter is associated with package motion and vortex shedding from the assemblies that hold the acoustic transducers. Similar devices (e.g. the Benthic Acoustic Stress Sensor, (e.g. Shaw *et al.* 2001) have been used for oceanic boundary layer turbulence studies while deployed from stable, but short (7 m-tall and less) bottom landers. In using these devices on standard moorings, package motion is introduced by vortex-induced strumming associated with flow past the mooring cable. At flow speeds of 20 cm s^{-1} and with a 3/16" cable diameter, the associated Strouhal frequency (6-8 Hz) exceeds the maximum sampling frequency of approximately 4 Hz, and thus this strumming-induced

package motion is aliased back into lower frequencies. The effective noise floor is 0.5-1.0 cm s^{-1}, with lower levels characterizing the vertical component. Power usage with a standard battery setup and a 45 day deployment dictated a 4 Hz sampling schedule of 2 seconds on and 8 seconds off, resulting in a 0.05 Hz effective Nyquist frequency.

A custom MAVS (referred to as Super-MAVS) was built with an RBR-soloT sensor, characterized by a fast response (0.1 s) thermistor, set to sample at 16 Hz and stream serial data to be captured by the MAVS. The custom RBR also included a 10 cm sensor sting, and the sensing element was placed within the 10 cm cube sampling volume of the MAVS. This approach was taken to minimize flow distortion and time-base offsets. A Vector-NAV VN-100 motion package completed the instrument upgrade. The maximum sampling rate as configured was 0.3 s (3.33 Hz). This MAVS was placed at 26 m H_{ab}. Unfortunately, two of the acoustic paths returned substandard data and we do not report on this sensor in the main text. The remaining data were sufficient, however, to demonstrate that accurate estimates of the temperature flux could, in this instance, be obtained by the standard configuration of mounting an SBE-37 microCAT CTD on the MAVS frame so that the CTD sensors were within 50 cm of the sampling volume of the MAVS: the $w'T'$ covariance (figures 3 and 4) occurs at apparent frequencies U/H_{ab} that are much smaller than U/sensor separation.

In general, the MAVS records were significantly shorter than intended. Post-cruise testing suggested pulsatile current draw at cold (-0.5° C) ambient temperatures seriously impacted the lithium battery chemistry and has led to the development of external battery packs.

Our estimates of dissipation rate ϵ were obtained by regressing observed spectra onto a model discussed in Shaw *et al.* (2001) that accounts for aliasing assuming a -5/3 spectrum folded about the effective Nyquist frequency and noise in the form of a constant spectral density (i.e. white noise). Effects of spatial averaging over the acoustic path lengths were not included as these are small given the effective Nyquist frequency. The regression was carried out over frequencies larger than U/H_{ab} with the criteria that the temperature spectrum had indeed achieved its intertial subrange form.

Nortek AquaDopps. The AquaDopp is a 3-beam acoustic Doppler current meter that provides point measurements of 3-axis (u,v,w) currents. The AquaDopp is widely used for long-term deployments in standard moored applications. These current meters were set so as to consume there batteries over 45 days, and this resulted in noise levels of 2 cm s^{-1} in horizontal (u, v) and 3 cm s^{-1} in vertical velocity after burst sampling for 2 seconds at 23 Hz once every 20 seconds.

SBE-37 MicroCAT CTDs. SeaBird SBE-37 conductivity-temperature-depth instruments were strapped to each mooring cage, except the bottom most, and set to sample every 6 s. The temperature sensors have a 0.5 second time response and effective 1/2 point at 4 times the Nyquist frequency.

SBE-39 temperature sensors. SeaBird SBE-39 temperature recorders were clamped onto the mooring wire at varying depth intervals, and set to sample every 6 s. The temperature sensors have a 0.5 second time response.

6. Appendix 2: Microstructure processing

The following re-processing of VMP-6000 microstructure data was performed for this work:

(i) Spectral estimates were obtained using 4 s transform intervals and piece lengths of 10's to 1000 m. This enabled the robust implementation of a Rockland Scientific coherent noise subtraction algorithm that utilizes accelerometers to quantify the vibrational noise

of the instrument. Experience suggests that using too short a piece length results in the subtraction of turbulence signals from the observations. The trade-off is that vertical resolution is degraded by choosing too long a piece length.

(ii) Depth intervals were selected on the basis of having limited structure in the T-S diagram. The rate of dissipation of thermal variance χ can be thought of as resulting from a combination of both diapycnal mixing and isopycnal stirring (Ferrari & Polzin 2005, e.g.). The diapycnal signature dominates when the T-S relation is linear and has little finescale variability. In our data set, the isopycnal signature tends to be most prominent at the knees of the T-S diagram.

(iii) The VMP-6000 has its own SeaBird CTD that is used for *in situ* calibration of the microstructure temperature and conductivity probes. For the VMP-6000 unit used here, the CTD was unpumped and hence of marginal use in calculating salinity, density and buoyancy frequency. The preceding quality-control statement requires having a coincident wire lowered CTD to complement the VMP-6000 profile.

(iv) Consistency between the data from the two shear probes is enforced with routine processing by rejecting depth segments where the variance from one probe exceeds that of the other probe by a significant factor (3-5). Biases in probe calibrations show up as variance estimates, and are plotted against each other in a scatter diagram (e.g. Polzin and Montgomery). Probe biases can result from multiple sources, apart from partial breakage of the piezo-ceramic sensor. The manufacturer reports a preliminary documentation of temperature-dependent calibrations with a magnitude of O(5-10% / 10°C) and indeterminate sign. The piezo-ceramic materials are also understood to have a pressure sensitivity of similar magnitude, but documenting high-pressure calibrations for this sensor is extremely challenging. As a pragmatic measure, we have enforced probe consistency by adjusting the calibration of the lower-responding probe, so that spectra within the dissipation range $k_1 \cong L_K^{-1}$ and greater match. Such adjustments were done for half the data, and amount to probe sensitivity increases of 25-50% for the low-reporting sensor.

(v) Spectral integration end-points were determined by visual inspection. This non-optimal method is much more robust at maximizing signal-to-noise ratios.

Using this approach, we targeted depth intervals with specific reference to water masses. Antarctic Bottom Water (AABW) is the deepest, and has a potential temperature $\theta < 0$ °C and neutral density $\gamma^n > 28.26$ kg m^{-3}. Lower Circumpolar Deep Water (LCDW) lies above, and is defined by $\gamma^n > 28.0$ kg m^{-3}. LCDW is separated into segments lying above and below the mid-depth potential temperature maximum, which represents the deep knee in the local T-S diagram. Upper Circumpolar Deep Water (UCDW) is less dense yet, and bounded above by the temperature minimum that is the base of the winter mixed layer. Winter Water (WW) lies above this temperature minimum. Stratification, accounted for as the non-dimensional metric N/f with Coriolis frequency f, is uniformly weak ($N/f \cong 3-5$) within AABW and LCDW. Our UCDW segments host stratification rates of $N/f \cong 20$.

The fall rate of the VMP-6000 is determined by a balance between negative buoyancy associated with ballast (steel weights) and drag associated with brushes as the top end. This instrument is highly damped, with the physical consequence that vehicle motions at periods longer than 4 s increasingly contaminate the shear probe data. We would have liked to take longer transform intervals to examine the ratio of kinetic and potential energy gradient spectra at larger scales, but that requires a more delicately balanced vehicle, such as the High Resolution Profiler (Schmit *et al.* 1988).

Caveats about thermistor time response corrections. The FP07 temperature microstructure sensor mounted on the VMP-6000 is a glass-covered thermistor, whose 7 ms

time response is generally considered as being dominated by diffusion of heat through the fluid dynamical boundary layerand characterized with a single-pole response that scales in a viscous regime as $U^{1/3}$. Neglected in this description is diffusion of heat through the glass covering and through the semiconducting material itself (Lueck *et al.* 1977). In situ estimates of the time constant (Polzin & Montgomery 1996, e.g.) are difficult to accomplish in a robust manner, as this requires both high R_{eb} and large $\mid R_\rho \mid$, which can be elusive within a single data set.

To avoid such vagaries, one can assume high-R_{eb} dynamics, truncate the temperature variance estimate at frequencies for which the probe response is not problematic, and then estimate the variance that is not resolved in a theoretical representation. Several such representations suggest themselves, (Batchelor 1959; Kraichnan 1968). We, as do Bogucki *et al.* (2012), regard Kraichnan as a more copacetic realization of observed spectra.

Two distinct efforts were taken to address the temperature data. First, we took data, calibrations and probe constants at face value and integrated to maximize signal variance. Second, we adjusted shear probe calibrations to obtain agreement between probes, integrated shear probe data to obtain ϵ, then integrated temperature probe data to 15 Hz with the nominal time constant (roughly 20 Hz) and added the temperature gradient variance in the Kraichnan spectrum at frequencies greater than 15 Hz. Our result that $\Gamma > 0.2$ is independent of method. The former procedure likely underestimates (biased) the temperature gradient variance. We have found that *in situ* estimates of thermistor time constants are generally greater than the nominal 0.007 s and the one-pole representation of the response function underestimates probe response deficits at frequencies of 50 Hz and larger.

REFERENCES

Abrahamsen, E. Povl, Meijers, Andrew J. S., Polzin, Kurt L., Naveira Garabato, Alberto C., King, Brian A., Firing, Yvonne L., Sallee, Jean-Baptiste, Sheen, Katy L., Gordon, Arnold L., Huber, Bruce A. & Meredith, Michael P. 2019 Stabilization of dense antarctic water supply to the atlantic ocean overturning circulation. *Nature Climate Change* **9**, 742–746.

Armi, Laurence 1978 Some evidence for boundary mixing in the deep ocean. *Journal of Geophysical Research: Oceans* **83**, 1971–1979.

Baines, Peter G 1997 *Topographic effects in stratified flows*. Cambridge university press.

Batchelor, George K 1959 Small-scale variation of convected quantities like temperature in turbulent fluid part 1. general discussion and the case of small conductivity. *Journal of Fluid Mechanics* **5** (1), 113–133.

Bogucki, D. J., Luo, H. & Domaradzki, J. A. 2012 Experimental evidence of the kraichnan scalar spectrum at high reynolds numbers. *Journal of Physical Oceanography* **42** (10), 1717–1728.

Brink, Kenneth H & Lentz, Steven J 2010 Buoyancy arrest and bottom ekman transport. part i: Steady flow. *Journal of Physical Oceanography* **40** (4), 621–635.

Ferrari, R., Mashayek, A., McDougall, T. J., Nikurashin, M. & Campin, J-M. 2016 Turning ocean mixing upside down. *Journal of Physical Oceanography* **46** (7), 2239–2261.

Ferrari, Raffaele & Polzin, Kurt L 2005 Finescale structure of the t–s relation in the eastern north atlantic. *Journal of Physical Oceanography* **35** (8), 1437–1454.

Garabato, A. C. Naveira, McDonogh, E. L., Stevens, D. P., Heywood, K. J. & Sanders, R. J. 2002 On the export of Antarctic Bottom Water from the Weddell Sea. *Deep Sea Research II* **49**, 4715–4742.

Garabato, Alberto C. Naveira, Williams, Adam P. & Bacon, Sheldon 2014 The three-dimensional overturning circulation of the southern ocean during the woce era. *Progress in Oceanography* **120**, 41 – 78.

Garabato, A. Naveira & et al. 2017 Rrs james cook cruise jr16005, 17 mar - 08 may 2017. the

dynamics of the orkney passage outflow (dynopo). Project report. National Oceanography Centre.

Gargett, A. E., Hendricks, P. J., Sanford, T. B., Osborn, T. R. & Williams, A. J. 1981 A composite spectrum of vertical shear in the ocean. *Journal of Physical Oceanography* **11**, 1258–1271.

Gargett, A. E., Osborn, T. R. & Nasmyth, P. W. 1984 Local isotropy and the decay of turbulence in a stratified fluid. *Journal of Fluid Mechanics* **144**, 231?280.

Garrett, Christopher 1979 Comment on "some evidence for boundary mixing in the deep ocean" by laurence armi. *Journal of Geophysical Research: Oceans* **84**, 5095–5095.

Garrett, Chris, MacCready, Parker & Rhines, Peter 1993 Boundary mixing and arrested ekman layers: Rotating stratified flow near a sloping boundary. *Annual Review of Fluid Mechanics* **25** (1), 291–323.

Garrett, Christopher & Munk, Walter 1972 Oceanic mixing by breaking internal waves. In *Deep sea research and oceanographic abstracts*, , vol. 19, pp. 823–832. Elsevier.

Gemmrich, Johannes R. & van Haren, Hans 2002 Internal wave band eddy fluxes above a continental slope. *Journal of Marine Research* **60**, 227–253.

Gregg, M.C., D'Asaro, E.A., Riley, J.J. & Kunze, E. 2018 Mixing efficiency in the ocean. *Annual Review of Marine Science* **10** (1), 443–473.

Gregg, M. C., Winkel, D. P. & Sanford, T. B. 1993 Varieties of fully resolved spectra of vertical shear. *Journal of Physical Oceanography* **23**, 124–141.

Heywood, K. J., Garabato, A. C. Naveira & Stevens, D. P. 2002 High mixing rates in the abyssal Southern Ocean. *Science* **415**, 1011–1014.

Holleman, R. C., Geyer, W. R. & Ralston, D. K. 2016 Stratified turbulence and mixing efficiency in a salt wedge estuary. *Journal of Physical Oceanography* **46** (6), 1769–1783.

Jackett, David R & McDougall, Trevor J 1997 A neutral density variable for the world?s oceans. *Journal of Physical Oceanography* **27** (2), 237–263.

Jullion, Loic, Garabato, Alberto C. Naveira, Bacon, Sheldon, Meredith, Michael P., Brown, Pete J., Torres-Valdes, Sinhue, Speer, Kevin G., Holland, Paul R., Dong, Jun, Bakker, Dorothee, Hoppema, Mario, Loose, Brice, Venables, Hugh J., Jenkins, William J., Messias, Marie-Jose & Fahrbach, Eberhard 2014 The contribution of the weddell gyre to the lower limb of the global overturning circulation. *Journal of Geophysical Research: Oceans* **119**, 3357–3377.

Kaimal, J.C., Wyngaard, J.C.J., Izumi, Y. & Coté, O.R. 1972 Spectral characteristics of surface-layer turbulence. *Quarterly Journal of the Royal Meteorological Society* **98** (417), 563–589.

Kaminski, AK & Smyth, WD 2019 Stratified shear instability in a field of pre-existing turbulence. *Journal of Fluid Mechanics* **862**, 639–658.

Kraichnan, Robert H 1967 Inertial ranges in two-dimensional turbulence. *The Physics of Fluids* **10** (7), 1417–1423.

Kraichnan, Robert H 1968 Small-scale structure of a scalar field convected by turbulence. *The Physics of Fluids* **11** (5), 945–953.

de Lavergne, Casimir, Madec, Gurvan, Le Sommer, Julien, Nurser, A. J. George & Naveira Garabato, Alberto C. 2016*a* The impact of a variable mixing efficiency on the abyssal overturning. *Journal of Physical Oceanography* **46** (2), 663–681.

de Lavergne, Casimir, Madec, Gurvan, Le Sommer, Julien, Nurser, A. J. George & Naveira Garabato, Alberto C. 2016*b* The impact of a variable mixing efficiency on the abyssal overturning. *Journal of Physical Oceanography* **46** (2), 663–681.

Ledwell, James R. 2018 Comment on 'abyssal upwelling and downwelling driven by near-boundary mixing'. *Journal of Physical Oceanography* **48** (3), 739–748.

Lindborg, Erik 2006 The energy cascade in a strongly stratified fluid. *Journal of Fluid Mechanics* **550**, 207–242.

Lueck, R. G., Hertzman, O. & Osborn, T. R. 1977 The spectral response of thermistors. *Deep Sea Research* **24**, 951–970.

Lvov, Yuri V, Polzin, Kurt L, Tabak, Esteban G & Yokoyama, Naoto 2010 Oceanic internal-wave field: theory of scale-invariant spectra. *Journal of Physical Oceanography* **40** (12), 2605–2623.

Mashayek, A., Caulfield, C. P. & Peltier, W. R. 2017 Role of overturns in optimal mixing in stratified mixing layers. *Journal of Fluid Mechanics* **826**, 522?552.

Mater, Benjamin D., Venayagamoorthy, Subhas K., St. Laurent, Louis & Moum, James N. 2015 Biases in thorpe-scale estimates of turbulence dissipation. part i: Assessments from large-scale overturns in oceanographic data. *Journal of Physical Oceanography* **45**, 2497–2521.

McDougall, T. J. 1987 Thermobaricity, cabbeling, and water-mass conversion. *Journal of Geophysical Research* **92**, 5448–5464.

McDougall, T. J. & Ferrari, R. 2017 Abyssal upwelling and downwelling driven by near-boundary mixing. *Journal of Physical Oceanography* **47** (2), 261–283.

Nash, Jonathan D. & Moum, James N. 2001 Internal hydraulic flows on the continental shelf: High drag states over a small bank. *Journal of Geophysical Research: Oceans* **106**, 4593–4611.

Naveira Garabato, Alberto C., Frajka-Williams, Eleanor E., Spingys, Carl P., Legg, Sonya, Polzin, Kurt L., Forryan, Alexander, Abrahamsen, E. Povl, Buckingham, Christian E., Griffies, Stephen M., McPhail, Stephen D., Nicholls, Keith W., Thomas, Leif N. & Meredith, Michael P. 2019 Rapid mixing and exchange of deep-ocean waters in an abyssal boundary current. *Proceedings of the National Academy of Sciences* **116** (27), 13233–13238.

Orsi, Alejandro H, Whitworth III, Thomas & Nowlin Jr, Worth D 1995 On the meridional extent and fronts of the antarctic circumpolar current. *Deep Sea Research Part I: Oceanographic Research Papers* **42** (5), 641–673.

Osborn, T. R. 1980 Estimates of the local rate of vertical diffusion from dissipation measurements. *Journal of Physical Oceanography* **10** (1), 83–89.

Osborn, Thomas R. & Cox, Charles S. 1972 Oceanic fine structure. *Geophysical Fluid Dynamics* **3** (1), 321–345.

Polzin, KurtL & Montgomery, EllynT 1996 Microstructure profiling with the high resolution profiler. In *Proc. Microstructure Sensor Workshop*, pp. 109–115. Citeseer.

Polzin, K. L. 1996 Statistics of the Richardson number: Mixing models and finestructure. *Journal of Physical Oceanography* **26**, 1409–1425.

Polzin, K. L. 2009 An abyssal recipe. *Ocean Modelling* **30**, 298–309.

Polzin, K. L., Garabato, A. C. Naveira, Abrahamsen, E. P., Jullion, L. & Meredith, M. P. 2014*a* Boundary mixing in orkney passage outflow. *Journal of Geophysical Research: Oceans* **119**, 8627–8645.

Polzin, Kurt L, Garabato, Alberto C Naveira, Huussen, Tycho N, Sloyan, Bernadette M & Waterman, Stephanie 2014*b* Finescale parameterizations of turbulent dissipation. *Journal of Geophysical Research: Oceans* **119** (2), 1383–1419.

Polzin, K. L., Kunze, E., Toole, J. M. & Schmitt, R. W. 2003 The partition of finescale energy into internal waves and subinertial motions. *Journal of Physical Oceanography* **33**, 234–238.

Polzin, K. L. & Lvov, Y. L. 2011 Toward regional characterizations of the oceanic internal wavefield. *Reviews of Geophysics* **49**.

Polzin, K. L., Speer, K., Toole, J. M. & Schmitt, R. W. 1996 Mixing in the Romanche Fracture Zone. *Nature* **380**, 54–57.

Polzin, K. L., Toole, J. M., Ledwell, J. R. & Schmitt, R. W. 1997 Spatial variability of turbulent mixing in the abyssal ocean. *Science* **276** (5309), 93–96.

Rhines, Peter B 1979 Geostrophic turbulence. *Annual Review of Fluid Mechanics* **11** (1), 401–441.

Riley, James J & Lelong, Marie-Pascale 2000 Fluid motions in the presence of strong stable stratification. *Annual review of fluid mechanics* **32** (1), 613–657.

Schmit, Raymond W, Toole, John M, Koehler, Richard L, Mellinger, Edward C & Doherty, Kenneth W 1988 The development of a fine-and microstructure profiler. *Journal of Atmospheric and Oceanic Technology* **5** (4), 484–500.

Shaw, W. J., Trowbridge, J. H. & Williams III, A. J. 2001 Budgets of turbulent kinetic energy and scalar variance in the continental shelf bottom boundary layer. *Journal of Geophysical Research: Oceans* **106** (C5), 9551–9564.

Shih, L. H., Koseff, J. R., Ivey, G. N. & Ferziger, J. H. 2005 Parameterization of turbulent

fluxes and scales using homogeneous sheared stably stratified turbulence simulations. *Journal of Fluid Mechanics* **525**, 193?214.

Sreenivasan, Katepalli R. 1995 On the universality of the kolmogorov constant. *Physics of Fluids* **7** (11), 2778–2784.

Sreenivasan, Katepalli R. 1996 The passive scalar spectrum and the obukhovcorrsin constant. *Physics of Fluids* **8** (1), 189–196.

Sukhatme, Jai & Smith, Leslie M 2008 Vortical and wave modes in 3d rotating stratified flows: random large-scale forcing. *Geophysical and Astrophysical Fluid Dynamics* **102** (5), 437–455.

Taylor, John R & Sarkar, Sutanu 2008 Stratification effects in a bottom ekman layer. *Journal of Physical oceanography* **38** (11), 2535–2555.

Thwaites, FT & Williams, AJ 1996 Development of a modular acoustic velocity sensor. In *OCEANS 96 MTS/IEEE Conference Proceedings. The Coastal Ocean-Prospects for the 21st Century*, , vol. 2, pp. 607–612. IEEE.

Wenegrat, Jacob O, Callies, Jörn & Thomas, Leif N 2018 Submesoscale baroclinic instability in the bottom boundary layer. *Journal of Physical Oceanography* **48** (11), 2571–2592.

Zakharov, V. E., Lvov, V. S. & Falkovich, G. 1992 *Kolmogorov Spectra of Turbulence*. Berlin: Springer-Verlag.